

Proton Probability Distribution in the O···H···O Low-Barrier Hydrogen Bond: A Combined Solid-State NMR and Quantum Chemical Computational Study of Dibenzoylmethane and Curcumin

Xianqi Kong,[†] Andreas Brinkmann,^{*,‡} Victor Tersikh,^{†,§} Roderick E. Wasylshen,^{*,||} Guy M. Bernard,^{||} Zhuang Duan,^{||} Qichao Wu,^{||} and Gang Wu^{*,†}

[†]Department of Chemistry, Queen's University, 90 Bader Lane, Kingston, Ontario, Canada K7L 3N6

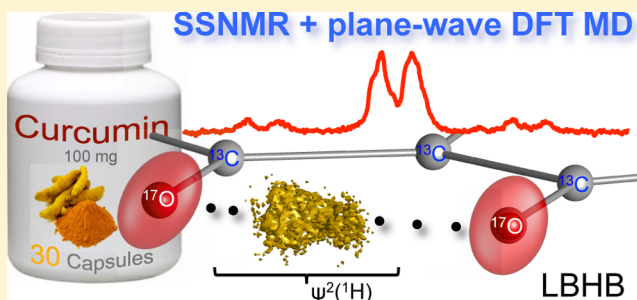
[‡]Measurement Science and Standards, National Research Council Canada, 1200 Montreal Road, M-40, Ottawa, Ontario, Canada K1A 0R6

[§]Department of Chemistry, University of Ottawa, 10 Marie Curie Private, Ottawa, Ontario, Canada K1N 6N5

^{||}Department of Chemistry, University of Alberta, Edmonton, Alberta, Canada T6G 2G2

Supporting Information

ABSTRACT: We report a combined solid-state (¹H, ²H, ¹³C, ¹⁷O) NMR and plane-wave density functional theory (DFT) computational study of the O···H···O low-barrier hydrogen bonds (LBHBs) in two 1,3-diketone compounds: dibenzoylmethane (1) and curcumin (2). In the solid state, both 1 and 2 exist in the *cis*-keto–enol tautomeric form, each exhibiting an intramolecular LBHB with a short O···O distance (2.435 Å in 1 and 2.455 Å in 2). Whereas numerous experimental (structural and spectroscopic) and computational studies have been reported for the enol isomers of 1,3-diketones, a unified picture about the proton location within an LBHB is still lacking. This work reports for the first time the solid-state ¹⁷O NMR data for the O···H···O LBHBs in 1,3-diketones. The central conclusion of this work is that detailed information about the probability density distribution of the proton (nuclear zero-point motion) across an LBHB can be obtained from a combination of solid-state NMR and plane-wave DFT computations (both NMR parameter calculations and *ab initio* molecular dynamics simulations). We propose that the precise proton probability distribution across an LBHB should provide a common basis on which different and sometimes seemingly contradicting experimental results obtained from complementary techniques, such as X-ray diffraction, neutron diffraction, and solid-state NMR, can be reconciled.



1. INTRODUCTION

Compounds containing the β -dicarbonyl fragment illustrate two important aspects of the hydrogen atom in chemistry, proton transfer and hydrogen bonding.^{1,2} For example, consider 2,4-pentanedione, better known by the common name acetylacetone (acac), which is often used to illustrate keto–enol tautomerism and intramolecular hydrogen bonding in undergraduate chemistry classes.^{3–5} In the enol isomer, one of the hydrogen atoms on the methylene carbon of the β -dicarbonyl fragment is transferred to one of the oxygen atoms where it is involved in hydrogen bonding (see Scheme 1). In the case of acac, and in fact most of the β -diketones, the enol tautomer seems to be favored over the keto isomer.^{6–8} Stabilization of the enol isomer is often attributed to intramolecular O···H···O hydrogen bonding. In addition, it has become popular to invoke resonance-assisted hydrogen bonding because of the formation of a six-membered “aromatic” ring involving the hydrogen-bonded proton.^{1,9,10} In the solid state, X-ray diffraction data for acac yielded an

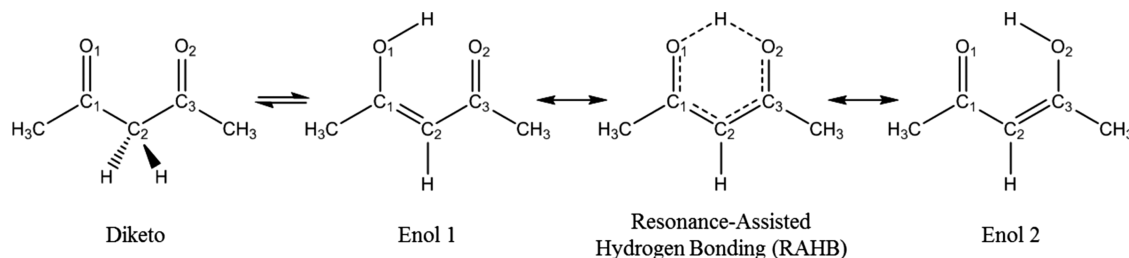
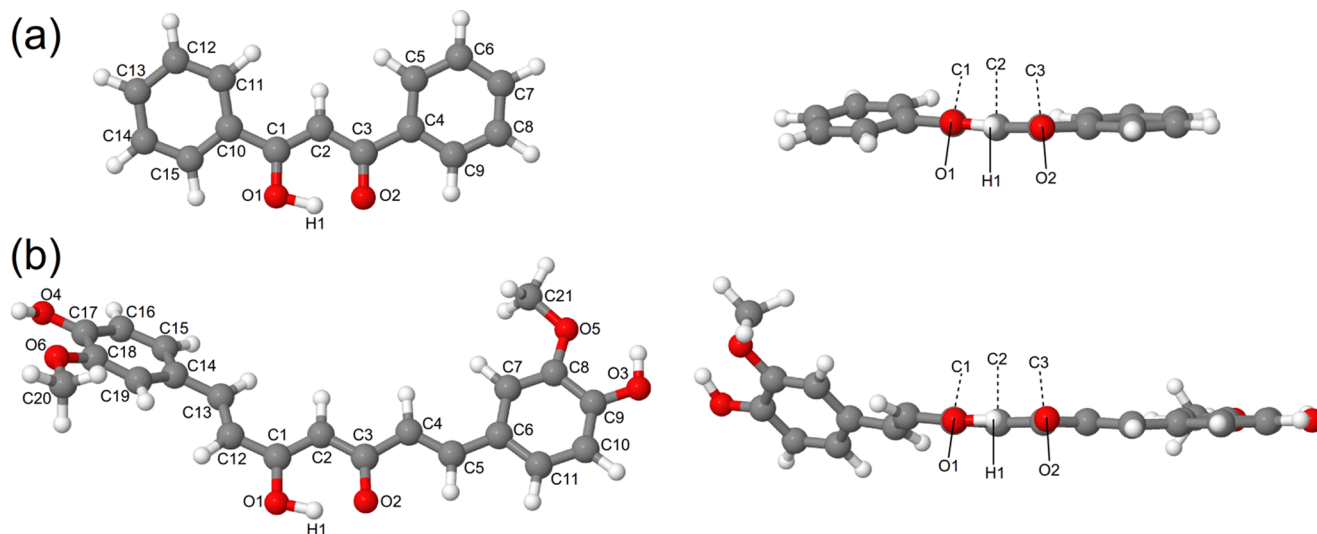
intramolecular O···O separation of 2.541(2) Å at 210 K and 2.547(1) Å at 110 K with the central hydrogen atom equally distributed over two positions near the oxygens.¹¹ That is, the diffraction data led to a picture where the hydrogen bond of acac has two distinct potential minima (i.e., a symmetric double-well potential). For many years now, it has been accepted that as the O···O separation in an intramolecular hydrogen bond decreases, the barrier separating the two potential minima also decreases until the potential barrier may be described by a single-well potential.^{12–14} In systems where the oxygen donor and acceptor separation r_{OO} is approximately between 2.4 and 2.6 Å, the zero-point energy is generally comparable to the potential barrier. Such hydrogen bonds have been classified as low-barrier hydrogen bonds (LBHBs); however, if $r_{OO} > 2.6$ Å, the hydrogen bond is generally

Received: August 10, 2016

Revised: October 25, 2016

Published: October 26, 2016

Scheme 1. Illustration of Different Tautomers in acac, a Typical 1,3-Diketone

Scheme 2. Top (Left) and Side (Right) Views of the Molecular Structures^a of (a) Dibenzoylmethane (1) and (b) Curcumin (2) Extracted from Their Crystal Structures^{19,35}

^aThe atomic numbering system used in this study is also shown. Note that for both 1 and 2, one-half (the right-hand side) of the molecule is coplanar with the *cis*-keto-enol core (H1–O1–C1–C2–C3–O2), whereas the other half is twisted out of the plane due to crystal packing.

classified as weak and if $r_{\text{OO}} < 2.4 \text{ \AA}$, the ground state (i.e., zero-point energy) will lie considerably above the barrier and the hydrogen bond is designated as very strong.¹⁴

Whereas without reviewing the extensive literature on hydrogen bonding in acac, we note that different pictures have emerged regarding the position of the hydrogen-bonded proton of acac depending on the technique used to characterize the hydrogen bond, probably a result of the time scale of the technique used to probe hydrogen bonding. For example, microwave data clearly showed that the enolic tautomer of acac has a C_{2v} symmetry.¹⁵ On the other hand, ultrafast electron diffraction data yielded an asymmetric ground-state structure.¹⁶ Quantum chemical calculations for acac at the CCSD(T)/aug-cc-pVDZ level predict a double-well potential with a barrier of 1276.7 cm^{-1} or $15.27 \text{ kJ mol}^{-1}$.¹⁷ For a linear OHO hydrogen bond where r_{OO} is $\approx 2.55 \text{ \AA}$, the two potential minima of the double-well potential energy curve are separated by $\approx 0.6 \text{ \AA}$; this separation is further reduced to $\approx 0.45 \text{ \AA}$ with a shorter r_{OO} of $\approx 2.45 \text{ \AA}$.¹⁴ Michaelides and co-workers have pointed out that in hydrogen-bonded systems the quantum nature of the proton (i.e., the H-atom) must be considered, as must zero-point motion, quantum delocalization, and quantum tunneling.¹⁸ More recently, McKenzie and co-workers have discussed the effect of quantum nuclear motion on hydrogen bonding, specifically in O–H \cdots O systems relevant to the current study.¹⁴ Clearly, our traditional view of hydrogen bonding and preoccupation that asks where the proton resides in a hydrogen

bond needs to consider the nuclear quantum effect. That is, one should ask about the probability distribution of the proton (i.e., the nuclear wavefunction), zero-point motion, quantum tunneling, and so forth.

The purpose of the present study is to combine experimental solid-state NMR (^1H , ^2H , ^{13}C , and ^{17}O) with plane-wave DFT computations to study two 1,3-diketone systems, both of which are in the enol form and exhibit LBHBs as previously characterized by diffraction techniques. One major limitation in many previous studies of LBHBs is that whereas experimental spectroscopic (NMR and IR) and structural (X-ray and neutron diffraction) data are often obtained for molecules in the condensed phases, the accompanying high-level computational studies are performed for isolated molecules in the gas phase. In this study, we avoid this pitfall by dealing exclusively with solid-state properties both experimentally and computationally. One of our goals is to suggest a new way of addressing the question of where the probability of finding the proton is greatest in an LBHB. The two solids that we have investigated are 1,3-diphenyl-1,3-propanedione (dibenzoylmethane, 1) and 1,7-bis(4-hydroxy-3-methoxyphenyl)-1,6-heptadiene-3,5-dione (curcumin, 2), a highly conjugated molecule consisting of two substituted phenols that are connected by an adjacent β -diketone fragment (see Scheme 2).

Dibenzoylmethane was chosen because it has been previously studied by both neutron and X-ray diffraction¹⁹ as

well as by solid-state ^1H and ^{13}C NMR.^{20–22} An early neutron diffraction study of dibenzoylmethane²³ suggests that the $\text{O}_1\cdots\text{O}_2$ separation is 2.463 (4) Å and that the enolic H atom is asymmetrically placed between the two O atoms, with the difference in O–H bond lengths being 0.199 (17) Å. In a more recent combined X-ray/neutron diffraction study of dibenzoylmethane, Wilson and co-workers highlighted the complementary nature of the two diffraction techniques,¹⁹ one being sensitive to the electronic density and the other to the nuclear density. In particular, their neutron data suggest that the enolic proton in dibenzoylmethane is asymmetrically located between the two O atoms and its position is insensitive to temperature, whereas the X-ray data show a gradual change of hydrogen bonding from being asymmetric at low temperatures to essentially symmetric at room temperature. Notably, solid-state NMR data should be sensitive to both the nuclear position and electronic structure in hydrogen bonding systems.^{24–28} However, a unified picture of the H atom behavior in an LBHB that can reconcile diffraction and solid-state NMR results is still lacking. In addition to the most stable orthorhombic polymorph (I) of dibenzoylmethane, two different polymorphs have also been reported in the literature.^{29,30}

Curcumin was selected in our study, in part because it is being touted as a wonder drug and is of intense interest to the pharmaceutical and medical community.^{31–33} The crystal structure of curcumin was first reported by Tønnesen et al., who used single-crystal X-ray diffraction at 121 K.³⁴ The $\text{O}_1\cdots\text{O}_2$ separation was found to be 2.446 Å, and the diffraction data were interpreted as having the enolic hydrogen with 50% occupancy at O_1 and O_2 , respectively. The authors of a more recent room-temperature X-ray diffraction study³⁵ concluded that within experimental accuracy the enolic hydrogen is localized at the midpoint between O_1 and O_2 . Curcumin has also been studied by solid-state ^{13}C NMR spectroscopy^{36–38} but there have been errors in assigning some of the peaks in some cases due to the presence of impurities in the sample. Whereas our peak assignments agree with Cornago et al.,³⁸ some of the assignments of Sanphui et al.³⁶ and Zhao et al.³⁷ are clearly incorrect (e.g., the peaks at 156.8 and 157.7 ppm that Sanphui et al. assigned to C1 and C17 are probably from bisdemethoxycurcumin; Zhao et al. made the same mistake but their shifts are given as 160.7 and 161.5 ppm). Three polymorphs of curcumin were reported by Sanphui et al. in 2011,³⁹ however, a 2015 paper by Liu et al.⁴⁰ raises questions about the conclusions concerning the polymorphs reported by Sanphui et al. The most stable and well-studied polymorph of curcumin is the monoclinic form, space group $P2_1/n$, that has been characterized in the above-mentioned X-ray diffraction papers.

2. MATERIALS AND METHODS

2.1. Sample Preparation. **2.1.1. [$^{17}\text{O}_2$]Dibenzoylmethane.** 1,3-Diphenyl-1,3-propanedione (336 mg) and ^{17}O -enriched water (41% ^{17}O -enrichment, 220 mg) were mixed in absolute ethanol (2 mL) and CDCl_3 (0.5 mL), followed by addition of Amberlite IR-120 strongly acidic resin (60 mg, prewashed). The mixture was heated at 55 °C (oil bath) for 2 days. After removal of the resin, the solution was concentrated (N_2 flow) to less than 1 mL with the formation of a white solid. The mixture was cooled in an ice–water bath for 10 min. The solid was collected (filtration), washed with cold methanol (3×1 mL), and dried under vacuum, giving the title compound as a white solid (260 mg). Solution ^{17}O NMR (67.68 MHz): 555.5

ppm (keto form, 3%) and 249.5 ppm (enol form, 97%). The ^{17}O -enrichment level in the compound was determined to be 19% by solution ^{17}O NMR.

2.1.2. [$^{17}\text{O}_2$]Curcumin. Commercial curcumin (Cat. No. B21573; Alfa Aesar) was recrystallized twice from methanol. It is important to emphasize that most commercial curcumins contain impurities, which have resulted in erroneous ^{13}C NMR assignments reported in the literature as mentioned earlier. The purified curcumin (200 mg) was dissolved in 17 mL MeOH (0.1% H_2O content), followed by addition of 40% ^{17}O -enriched water (200 mg) and prewashed Amberlite IR-120 ion-exchange resin (strongly acidic form, 100 mg). The mixture was kept at 65 °C (oil bath) for 3 h. After the resin was removed, the mixture was concentrated to a small volume. The solid was collected, washed with cold water (4 mL) and ether (3×1 mL), and dried under vacuum, giving the title compound as an orange–yellow solid (165 mg). The ^{17}O -enrichment level in the compound was determined to be 17% by solution ^{17}O NMR.

2.1.3. [^2H]Dibenzoylmethane and [^2H]Curcumin. Dibenzoylmethane was recrystallized from methanol- d_4 . Whereas the final [^2H]-1 sample contains both dibenzoylmethane- d_1 and - d_2 , the level of deuteration at the $\text{O}\cdots\text{D}\cdots\text{O}$ site is nearly 100%, as determined from the C1 and C3 signals in the ^{13}C cross-polarization magic-angle spinning (CP/MAS) spectrum as well as the ^1H MAS spectrum of the compound. Curcumin was recrystallized from ethanol- d_1 . The final [^2H]-2 sample contains ^2H -labeling at multiple sites because of the presence of two phenol groups in 2. The level of deuteration at the $\text{O}\cdots\text{D}\cdots\text{O}$ site is about 40%.

2.2. Solid-State NMR. Deuterium and ^{13}C NMR spectra were obtained at 7.05 or 11.75 T at the University of Alberta on Bruker Avance 300 or 500 spectrometers, using Bruker 4 mm MAS probes operating in double-resonance mode. Carbon-13 NMR spectra were obtained with CP using contact times of 3.0–4.0 ms, 90° degree ^1H pulses of 4.0 μs , recycle delays of 5 s (for curcumin) or 15 s (for dibenzoylmethane), and MAS frequencies of 8.0–10.0 kHz. The ^2H NMR spectrum for curcumin was obtained at 11.75 T under the CP condition with a 5.0 ms contact time, a 20.0 s recycle delay, and a sample spinning frequency of 5.0 kHz and that for dibenzoylmethane was obtained at 7.05 T with direct polarization, an MAS frequency of 3.0 kHz, and a recycle delay of 120.0 s. Solid-state ^{13}C NMR spectra of dibenzoylmethane and curcumin were also obtained at 21.1 T. The static ^{17}O NMR spectra at 14.1 T were recorded on a Bruker Avance 600 spectrometer at Queen's University. The static and MAS ^{17}O NMR spectra at 21.1 T were obtained on a Bruker Avance II 900 spectrometer at the National Ultrahigh-field NMR Facility for Solids, Ottawa, Canada. At 21.1 T, the static experiments were carried out on a 5 mm home-built double-channel H/X solenoid probe and the MAS experiments were conducted using a 3.2 mm Bruker double-channel H/X MAS probe. In static experiments, powder samples were packed into a Teflon tube (Norell) to minimize the unwanted ^{17}O background signal. The ^1H MAS spectra were obtained at 21.1 T with a 4 mm Bruker HCN probe. Simulations of ^{17}O NMR spectra were performed with DMfit.⁴¹ Carbon-13 CP/MAS spectra of all samples of curcumin used in this study, including the ^{17}O - and ^2H -labeled samples, are nearly identical, confirming that they are all in the most stable monoclinic polymorph. All chemical shifts are tabulated in the Supporting Information.

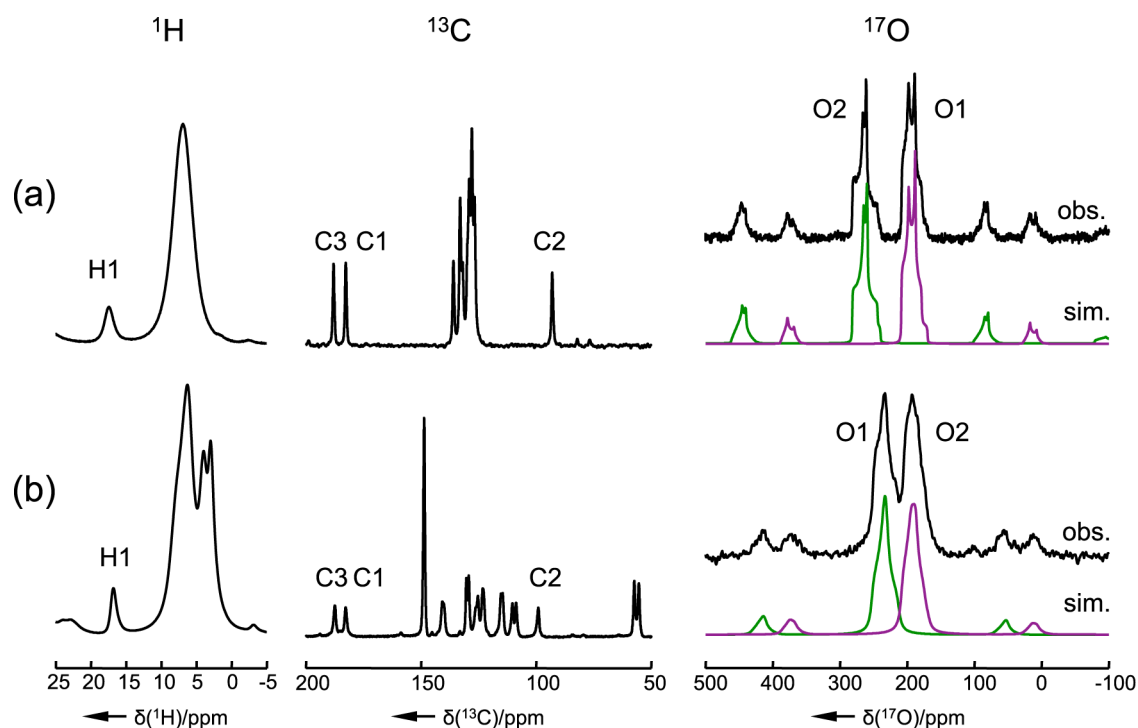


Figure 1. Solid-state ^1H , ^{13}C , and ^{17}O NMR spectra of (a) **1** and (b) **2**. The ^1H (18 kHz) and ^{17}O (22 kHz) MAS spectra were obtained at 21.1 T. The ^{13}C CP/MAS spectra for **1** and **2** were recorded at 7.05 T. See [Materials and Methods](#) for details.

2.3. Quantum Chemical and Molecular Dynamics (MD) Calculations. All quantum chemical and MD calculations were performed using the Cambridge Sequential Total Energy Package (CASTEP) code (versions 7.0 and 8.0)⁴² together with BIOVIA's Materials Studio. CASTEP employs DFT using the plane-wave pseudopotential approach. For all calculations in this work, the generalized gradient approximation with the Perdew–Burke–Ernzerhof exchange correlation functional⁴³ was chosen. The NMR parameters were calculated using the gauge including the projector augmented waves (GIPAW) method implemented in the NMR module of CASTEP.^{44,45} In the following, further computational details are given.

Dibenzoylmethane (1). The crystal structure of dibenzoylmethane determined by neutron diffraction at 100 K¹⁹ was used as the starting point for the geometry optimization of different tautomers, for which the Broyden–Fletcher–Goldfarb–Shanno (BFGS) algorithm, ultrasoft pseudopotentials, a cutoff energy of 300 eV, and a $2 \times 2 \times 1$ k -point grid were chosen. Tautomers corresponding to local energy minima were fully geometry optimized. The transition state was searched using the complete linear synchronous transit/quadratic synchronous transit (LST/QST) protocol with a maximum ionic force and displacement tolerances of 0.25 eV/Å and 10^{-3} Å, respectively, using ultrasoft pseudopotentials with a cutoff energy of 340 eV and a $2 \times 1 \times 1$ k -point grid. The NMR parameters were calculated by GIPAW-DFT calculations using “on-the-fly” pseudopotentials together with a plane-wave cutoff energy of 550 eV and a $3 \times 2 \times 1$ k -point grid. The MD calculation in CASTEP was performed in three steps: (1) fully optimize the geometry of the molecule, (2) perform a MD run until thermal equilibrium is reached, and finally (3) perform the actual MD calculation. For all of the three steps, ultrasoft pseudopotentials together with a cutoff energy of 300 eV and a $2 \times 1 \times 1$ k -point grid were chosen. All MD calculations used an integration time

step of 1.0 fs, a fixed center of mass, and the canonical (NVT) ensemble held at a constant temperature of 280 K employing a Langevin thermostat. The MD run to thermal equilibrium lasted a total of 0.7 ps using a thermostat time constant of 0.1 ps. The total simulation time of the actual MD calculation was 5 ps, where a thermostat time constant of 0.5 ps was used, resulting in a mean temperature of 285.4 K with a standard deviation of 12.3 K. The complete MD run took 16 days on a dual Intel Xeon six-core 2.93 GHz processor workstation.

Curcumin (2). Tautomers of curcumin were geometry optimized in CASTEP starting from the structure determined by single-crystal XRD.³⁵ For geometry optimization, the BFGS algorithm together with ultrasoft pseudopotentials, a plane-wave cutoff energy of 300 eV, and a $1 \times 2 \times 1$ k -point grid was chosen. Geometry optimizations for stable tautomers and the transition-state structure were performed in the same way as described earlier for dibenzoylmethane. The transition state search was conducted using the complete LST/QST protocol with a maximum ionic force and displacement tolerances of 0.25 eV/Å and 10^{-3} Å, respectively, using ultrasoft pseudopotentials with a cutoff energy of 340 eV and a $1 \times 2 \times 1$ k -point grid. The GIPAW-DFT calculations of the NMR parameters were performed using on-the-fly pseudopotentials together with a plane-wave cutoff energy of 550 eV and a $2 \times 3 \times 1$ k -point grid. For the MD calculations, ultrasoft pseudopotentials, a cutoff energy of 300 eV, a $1 \times 2 \times 1$ k -point grid, and a temperature of the NVT ensemble of 300 K were used. All other MD parameters were identical to those used for dibenzoylmethane. The mean temperature amounted to 303.7 K with a standard deviation of 16.9 K. The complete MD run took 8 days on a dual Intel Xeon six-core 2.93 GHz processor workstation.

Table 1. Comparison between Experimental Solid-State NMR Parameters and Plane-Wave DFT Computational Results^{a,b} for 1 and 2

molecule	atom		computational model				expt.
			A	AB	B	$\langle A + B \rangle^c$	
dibenzoylmethane (1)	H1	$\delta_{\text{iso}}/\text{ppm}$	19.0	20.4	18.8	18.9	17.5
		C_Q/kHz	58	23	62	−47	101
		η_Q	0.57	0.75	0.56	0.87	0.53
	C1	$\delta_{\text{iso}}/\text{ppm}$	183.0	187.9	191.7	187.3	188.0
	C2	$\delta_{\text{iso}}/\text{ppm}$	94.9	94.1	93.6	94.2	92.9
	C3	$\delta_{\text{iso}}/\text{ppm}$	190.9	187.8	183.3	187.1	182.7
	O1	$\delta_{\text{iso}}/\text{ppm}$	196	254	322	259	210
		δ_{11}/ppm	353	413	558	423	367
		δ_{22}/ppm	266	383	452	391	307
		δ_{33}/ppm	−32	−34	−43	−37	−38
		C_Q/MHz	−6.8	−6.4	7.1	−6.4	−6.2
		η_Q	0.17	0.68	0.71	0.72	0.50
		$\delta_{\text{iso}}/\text{ppm}$	321	258	197	259	282
		δ_{11}/ppm	554	432	370	435	480
		δ_{22}/ppm	465	386	263	391	401
		δ_{33}/ppm	−55	−45	−42	−48	−47
		C_Q/MHz	7.1	−6.3	−6.8	−6.4	−6.2
		η_Q	0.69	0.73	0.20	0.74	0.76
	O2	$\delta_{\text{iso}}/\text{ppm}$	16.0	19.5	18.2	17.1	16.8
		C_Q/kHz	99	26	49	58	100
		η_Q	0.32	0.13	0.64	0.83	0.53
		$\delta_{\text{iso}}/\text{ppm}$	181.2	189.7	192.6	186.9	187.4
		$\delta_{\text{iso}}/\text{ppm}$	103.2	102.8	102.8	103.0	99.0
		$\delta_{\text{iso}}/\text{ppm}$	187.3	181.6	178.0	182.6	182.7
		$\delta_{\text{iso}}/\text{ppm}$	183	280	332	257	252
		δ_{11}/ppm	325	439	556	404	393
		δ_{22}/ppm	221	399	444	368	367
		δ_{33}/ppm	2	3	−4	0	−10
curcumin (2)	H1	$\delta_{\text{iso}}/\text{ppm}$	16.0	19.5	18.2	17.1	16.8
		C_Q/kHz	99	26	49	58	100
		η_Q	0.32	0.13	0.64	0.83	0.53
	C1	$\delta_{\text{iso}}/\text{ppm}$	181.2	189.7	192.6	186.9	187.4
	C2	$\delta_{\text{iso}}/\text{ppm}$	103.2	102.8	102.8	103.0	99.0
	C3	$\delta_{\text{iso}}/\text{ppm}$	187.3	181.6	178.0	182.6	182.7
	O1	$\delta_{\text{iso}}/\text{ppm}$	183	280	332	257	252
		δ_{11}/ppm	325	439	556	404	393
		δ_{22}/ppm	221	399	444	368	367
		δ_{33}/ppm	2	3	−4	0	−10
		C_Q/MHz	−7.2	−6.4	6.9	−6.6	−6.0
		η_Q	0.23	0.70	0.82	0.52	0.90
		$\delta_{\text{iso}}/\text{ppm}$	272	192	156	214	209
		δ_{11}/ppm	464	329	296	345	337
		δ_{22}/ppm	394	272	200	332	313
		δ_{33}/ppm	−41	−26	−27	−33	−35
		C_Q/MHz	−6.9	−7.1	−7.4	−7.0	−6.2
		η_Q	0.91	0.15	0.16	0.36	0.65
	O2	$\delta_{\text{iso}}/\text{ppm}$	272	192	156	214	209
		δ_{11}/ppm	464	329	296	345	337
		δ_{22}/ppm	394	272	200	332	313
		δ_{33}/ppm	−41	−26	−27	−33	−35
		C_Q/MHz	−6.9	−7.1	−7.4	−7.0	−6.2
		η_Q	0.91	0.15	0.16	0.36	0.65

^aTo convert the computed magnetic shielding values into chemical shifts, the following σ_{ref} values were used: ^1H , 29.0; ^{13}C , 170.4; ^{17}O , 287 ppm. The uncertainties in experimental results are $\delta_{\text{iso}}(^1\text{H})$, ± 0.1 ppm; $\delta_{\text{iso}}(^{13}\text{C})$, ± 0.1 ppm; $\delta_{\text{iso}}(^{17}\text{O})$, ± 2 ppm; $\delta_{\text{ii}}(^{17}\text{O})$, ± 10 ppm; $C_Q(^2\text{H})$, ± 5 kHz; $C_Q(^{17}\text{O})$, ± 0.1 MHz. ^bThe sign of $C_Q(^{17}\text{O})$ was assumed to be the same as that of the computed one. ^cEqual populations were assumed between A and B. The full chemical shift or electric-field gradient tensors were first averaged in the Cartesian coordinate system and then diagonalized to yield the averaged principal tensor components.

3. RESULTS AND DISCUSSION

3.1. Experimental ^1H , ^2H , ^{13}C , and ^{17}O NMR Parameters. Figure 1 shows the solid-state ^1H , ^{13}C , and ^{17}O NMR spectra obtained under MAS conditions for 1 and 2. The isotropic ^1H chemical shifts for the protons involved in the $\text{O}\cdots\text{H}\cdots\text{O}$ HBs in 1 and 2 are 17.5 and 16.8 ppm, respectively. These ^1H chemical shifts are characteristic of the LBHB formation.² For 1, Emmmler et al. and Etter et al. reported a ^1H chemical shift of 18.1 ppm.^{20,46} In the ^{13}C CP/MAS spectra of 1 and 2, shown in Figure 1, the most interesting feature is that the C1 and C3 atoms display different ^{13}C chemical shifts: 182.7 and 188.0 ppm in 1; 182.7 and 187.4 ppm in 2. For 1, Vila et al. previously reported ^{13}C chemical shifts for C1 and C3 of 182.9 and 188.2 ppm, respectively,²² whereas Etter et al. reported 182.3 and 187.6 ppm.²¹

Similar to the ^{13}C NMR observations, the two oxygen atoms in each of the $\text{O}\cdots\text{H}\cdots\text{O}$ LBHBs in 1 and 2 also display different chemical shifts. As seen from Figure 1, the ^{17}O MAS spectra contain two signals each displaying a characteristic line shape arising from the second-order quadrupole interaction. From simulations of the ^{17}O MAS spectra, we can obtain three ^{17}O NMR parameters (δ_{iso} , C_Q , and η_Q) for each oxygen atom. Detailed results are given in Table 1. Note that the assignments of C1 and C3 and O1 and O2 are based on the DFT calculations (vide infra). Interestingly, the ^{17}O chemical shift differences between the two oxygen atoms in 1 and 2 are 72 and 43 ppm, respectively. These are considerably greater than the corresponding ^{13}C chemical shift differences observed in these compounds, 5.3 and 4.7 ppm. Furthermore, the observed difference in the ^{17}O and ^{13}C chemical shift differences is about 3 times larger than that normally expected from the chemical

shift ranges for ^{17}O and ^{13}C nuclei. For example, if we use the ratio of $\langle 1/r^3 \rangle_{2p}$ between O and C atoms as a measure of the chemical shift range, as demonstrated by Jameson and Gutowsky,⁴⁷ $\langle 1/r^3 \rangle_{2p}(\text{O})/\langle 1/r^3 \rangle_{2p}(\text{C})$ is only 3.5.⁴⁸ This illustrates the extraordinary sensitivity of ^{17}O NMR to the hydrogen bonding. Of course, it is the oxygen that is involved in the H-bond, whereas the carbon is more of a spectator. The enhanced sensitivity of ^{17}O NMR over ^{13}C NMR was previously reported for both hydrogen bonding and ion–carbonyl interactions.⁴⁹ We note that the C_Q values appear to be very similar for the two oxygen atoms in each of the two compounds.

The observed ^{17}O NMR parameters for **1** and **2** are drastically different from those expected for isolated keto and enol functional groups. For example, Zhu et al. reported that the keto oxygen atom in sodium pyruvate has $\delta_{\text{iso}} = 543$ ppm and $C_Q = +10.8$ MHz.⁵⁰ Whereas there is no solid-state ^{17}O NMR study of the enol functional group in the literature, the phenolic oxygen can be considered to be a close analogue. Zhu et al. reported that the phenolic oxygen in L-tyrosine displays $\delta_{\text{iso}} = 81$ ppm and $C_Q = -8.5$ MHz.⁵¹ As expected, the ^{17}O NMR parameters observed for 1,3-diketones lie somewhere in between those for isolated keto and enol functional groups (vide infra).

To fully characterize the ^{17}O CS tensors in **1** and **2**, we obtained solid-state ^{17}O NMR spectra under the static condition at two magnetic fields, 14.1 and 21.1 T. As seen from Figure 2, the static spectra obtained at the two fields can be simultaneously fitted using the same set of parameters and the agreement between the experimental and simulated spectra is reasonable. From this kind of spectral analysis, one can extract not only the principal components of the ^{17}O CS tensor but also the relative orientation between the CS and QC tensors in the molecular frame of reference.⁵² The results for

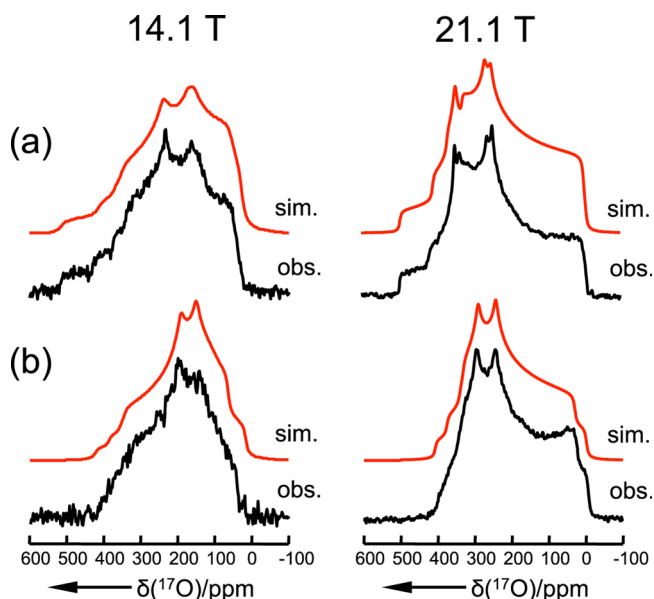


Figure 2. Experimental (black trace) and simulated (red trace) static ^{17}O NMR spectra of (a) $^{17}\text{O}_2$ -**1** and (b) $^{17}\text{O}_2$ -**2** at two magnetic fields. The NMR tensor parameters used in the simulations are given in Table 1. The relative orientations between the ^{17}O QC and CS tensors are **1**(O1), $\alpha = 8 \pm 5^\circ$, $\beta = 86 \pm 5^\circ$, $\gamma = 0 \pm 5^\circ$, **1**(O2), $\alpha = 0 \pm 5^\circ$, $\beta = 82 \pm 5^\circ$, $\gamma = 90 \pm 5^\circ$; **2**(O1), $\alpha = 0 \pm 5^\circ$, $\beta = 80 \pm 5^\circ$, $\gamma = 0 \pm 5^\circ$, **2**(O2), $\alpha = 0 \pm 5^\circ$, $\beta = 80 \pm 5^\circ$, $\gamma = 90 \pm 5^\circ$.

the ^{17}O CS tensor components for **1** and **2** are reported in Table 1. The two oxygen atoms in each compound have somewhat different ^{17}O CS anisotropies. For example, the ^{17}O CS tensors for O1 and O2 in **1** have spans ($\delta_{11} - \delta_{33}$) of 405 and 527 ppm, respectively. These values can be compared to the corresponding results reported for isolated keto (1060 ppm) and phenol (77 ppm) functional groups. Once again, the ^{17}O CS anisotropies of 1,3-diketones can be considered to be the “averaged” values between keto and phenol groups.

To gain more information about the $\text{O} \cdots \text{H} \cdots \text{O}$ LBHBs in **1** and **2**, we prepared two ^2H -labeled samples. Figure 3 shows the ^2H MAS spectra obtained for ^2H -**1** and ^2H -**2** at 294 K. Because, in general, the enolic C–H moiety in a 1,3-diketone can undergo proton/deuteron exchange, each ^2H NMR spectrum contains more than one signal in the isotropic region. The ^2H NMR spectrum of $^{[2]\text{H}}$ -**2** is further complicated by the presence of two additional phenolic groups, which are crystallographically inequivalent in the solid state. Nonetheless, as seen from Figure 3, the ^2H NMR signals associated with the $\text{O} \cdots \text{D} \cdots \text{O}$ LBHBs are well separated from other signals, allowing reliable determination of the ^2H quadrupole parameters for $^{[2]\text{H}}$ -**1** and $^{[2]\text{H}}$ -**2**. We obtained the following results for the $\text{O} \cdots \text{D} \cdots \text{O}$ site: **1**, $C_Q(^2\text{H}) = 101 \pm 5$ kHz, $\eta_Q = 0.53 \pm 0.05$; **2**, $C_Q(^2\text{H}) = 100 \pm 5$ kHz, $\eta_Q = 0.53 \pm 0.05$. For **1**, Brown et al. reported a ^2H NQR study where they obtained $C_Q(^2\text{H}) = 115.3(13)$ kHz and $\eta_Q = 0.26(4)$ at 300 K.⁵³ Whereas our $C_Q(^2\text{H})$ value is slightly smaller than their value, the value of η_Q is significantly different from theirs. Harbison et al. also used solid-state ^2H NMR to examine **1** and reported a C_Q value of 104 kHz at 300 K;⁵⁴ however, they did not report the η_Q value. Whereas it is unclear as to the origin of the discrepancy between our ^2H NMR data and those reported by Brown et al., our solid sample of $^{[2]\text{H}}$ -**1** produces a ^{13}C CP/MAS spectrum that is nearly identical to that from both the natural abundance and ^{17}O -labeled samples of **1**. These data strongly indicate that all our solid samples of **1** are for the most stable orthorhombic polymorph (**I**).²³ The magnitudes of $C_Q(^2\text{H})$ found for **1** and **2** seem to lie between two extremes: one being around 50–80 kHz often found for strongly hydrogen-bonded systems (e.g., KH maleate) and the other being around 160–200 kHz for regular C–O–D moieties involving weak HBs.⁵⁵ This trend is also parallel to that in the ^1H chemical shifts for **1** and **2**. It is also interesting to note that, for **1**, $C_Q(^2\text{H})$ exhibits a very weak negative temperature dependence (-0.020 kHz/K),⁵⁴ which is in contrast to those found for very short HBs (e.g., KH maleate). For **2**, we found that the ^2H NMR spectra obtained in the temperature range between 293 and 360 K are virtually identical, suggesting that $C_Q(^2\text{H})$ is rather insensitive to temperature. These results suggest that the hydrogen bonding interactions in **1** and **2** are distinct from those seen in either very short or regular HBs.

3.2. Evaluation of Various Structural Models and Hydrogen Bonding Potential Energy Surfaces (PESs). To better understand the observed NMR parameters, especially the ^{17}O NMR tensors, we performed quantum chemical calculations utilizing the CASTEP code, which is based on a DFT approach and employs a plane-wave basis set for computing various properties of crystalline solids.⁴² In general, before one carries out a plane-wave DFT computation for NMR parameters, it is important to evaluate various structural models. That is, whether one should use the crystal structure reported from either X-ray or neutron diffraction studies or

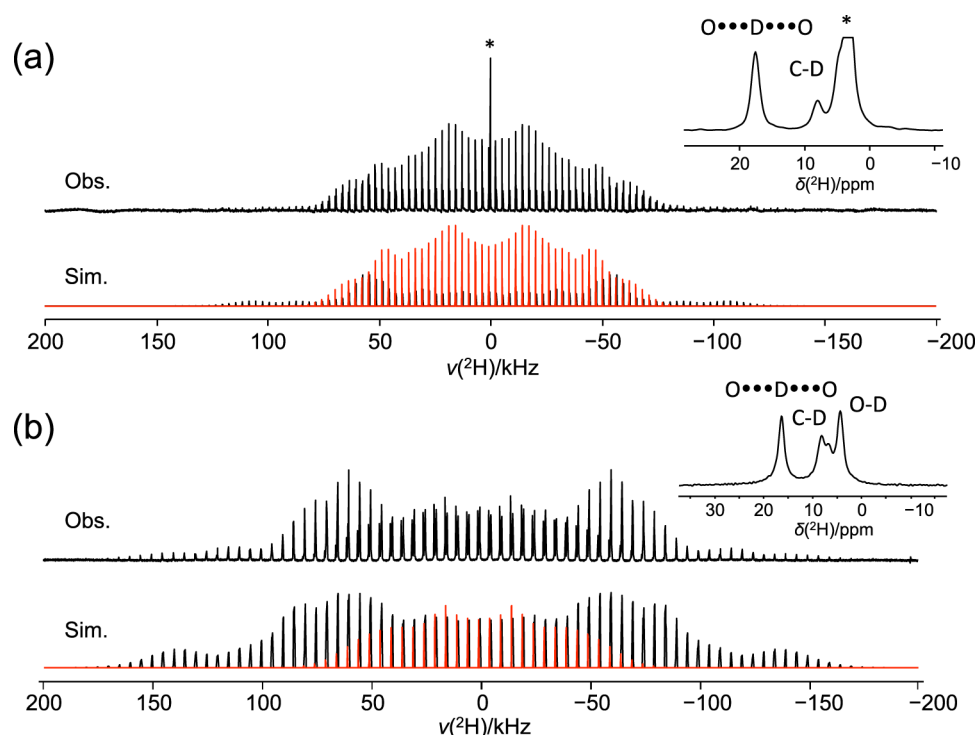


Figure 3. Observed and simulated ^2H MAS spectra of (a) $[\text{}^2\text{H}]\text{-1}$ and (b) $[\text{}^2\text{H}]\text{-2}$ at 294 K. The isotropic peaks are shown in insets. The signals associated with the $\text{O}\cdots\text{D}\cdots\text{O}$ LBHBs are shown in red. In (a), the signal from residual methanol- d_4 is marked by *. The sample spinning frequency was (a) 3.0 and (b) 5.0 kHz.

whether one should perform a full geometry optimization.⁵⁶ This step is particularly important for 1,3-diketones, such as **1** and **2**, as the proton location in these systems is often not very well defined from diffraction studies, as mentioned earlier. Here, starting from the best crystal structures available for **1** and **2**,^{19,35} we evaluated the following three structural models. In model A, H1 is directly bonded to O1, while performing geometry optimization (i.e., $\text{O1-H1}\cdots\text{O2}$). As seen from Scheme 2, in this model, the protonated enol oxygen (O1) is on the side of the half molecule that is twisted out of the plane of the *cis*-keto-enol core (H1-O1-C1-C2-C3-O2). In model B, H1 is directly bonded to O2 while performing geometry optimization (i.e., $\text{O1}\cdots\text{H1-O2}$). Now the protonated enol oxygen (O2) is on the side of the half molecule that is co-planar with the *cis*-keto-enol core. The plane-wave DFT calculations suggest that both A and B represent local energy minima. Model AB was obtained as the true transition state connecting models A and B. For **1**, the $\text{O1}\cdots\text{O2}$ distances for models A, AB, and B were found to be 2.402, 2.403, and 2.405 Å, respectively. For **2**, the variations in the $\text{O1}\cdots\text{O2}$ distances among the three models are slightly larger (2.430, 2.442, and 2.467 Å for A, AB, and B, respectively). These results appear to be different from those reported for acac in the gas phase for which the $\text{O}\cdots\text{O}$ distance in the C_{2v} transition-state structure (2.372 Å) is significantly shorter than that in the C_s ground-state structure (2.575 Å).¹⁷ We speculate that two factors may be in play here. First, the barrier heights in **1** (1.1 kJ mol^{-1}) and **2** (5.3 kJ mol^{-1}) are significantly smaller than those seen in acac (15.3 kJ mol^{-1}). Thus, it is perhaps reasonable to expect a diminishing difference between the ground and transition states in **1** and **2**. Second, the crystal packing in **1** and **2** may impose additional restrictions for the degrees of freedom available for the *cis*-keto-enol core as compared to those available for

isolated molecules of acac in the gas phase. The other structural details around the intramolecular HBs and relative energy values for the three models are shown in Figure 4. Immediately, one can see that the computed energy barriers for proton

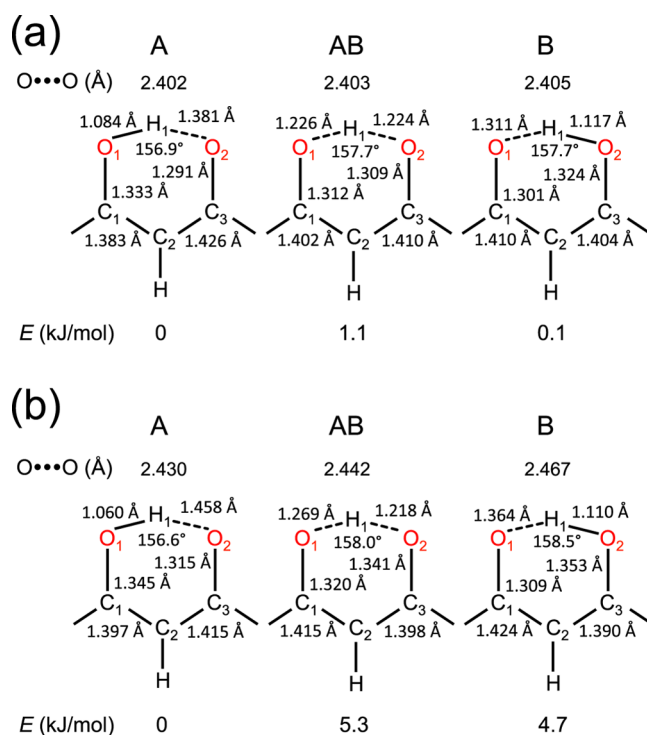


Figure 4. Selected structural parameters of the *cis*-keto-enol cores and relative energy values of models A, AB, and B for (a) **1** and (b) **2**.

transfer in **1** and **2** are quite small. In addition, our plane-wave DFT calculations suggest that model A is the global ground state for **1**, which is in agreement with the crystal structure of **1**¹⁹ and the results from a similar DFT calculation by Deringer et al.⁵⁷ Likewise, the calculations for **2** suggest that A is also more stable, but in this case the difference between A and B is greater, 4.7 kJ mol⁻¹. This is different from that reported in the crystal structure of **2** by Parimita et al.²⁸ They suggested that the enolic proton is closer to O2 than to O1, which resembles more than that seen in model B. Close inspection of the crystal structure of **2** reveals the presence of an intermolecular HB between O2 and the phenolic group O4–H, as illustrated in Figure 5. We speculate that the HB network of a keto oxygen

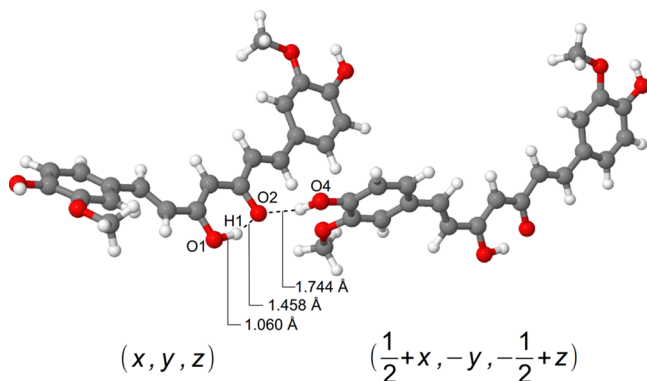


Figure 5. Two symmetry-related molecules in the crystal lattice of curcumin (**2**) (model A). Both intra- and intermolecular hydrogen bonds and their respective distances are shown.

(O2) simultaneously accepting two HBs (as in model A) may be slightly preferred over an enol group (O2–H1), being both a HB donor and an acceptor (as in model B). Similar situations were previously seen in salicylic acid crystals⁵⁸ and in a MeOH solution of dibenzoylmethane.⁵⁹ Of course, this conclusion is based entirely on the energies calculated using the plane-wave DFT methodology described in Section 2.3. Further investigations are required to clarify this picture with certainty.

Now given the fact that plane-wave DFT computations predict shallow energy barriers for proton transfer in both **1** and **2**, a fundamental question is whether H1 should be viewed as being bonded to either O1 or O2 or being shared between O1 and O2. It is well known that the probability density distribution of the proton depends critically on the shape of the PES. For this reason, before we present a detailed analysis of the computed NMR parameters from the three structural models, we wish to gain some insights into the PES in **1** and **2**. Whereas we recognize that the O1...H1...O2 HBs in **1** and **2** are far from being linear (the O1–H1–O2 angles being <160°), it is still instructive as a first step to reduce this problem to a simple one-dimensional (1D) model where the HB is assumed to be linear. Figure 6 shows such simplified 1D potential energy curves. The 1D potential energy curves were modeled with polynomial functions, each passing the three stationary points obtained from CASTEP calculations for the aforementioned three models. With these potential energy curves, we solved the 1D Schrödinger equation using the Numerov method⁶⁰ and obtained the 1D nuclear wavefunctions for both ground and excited states. As seen from Figure 6, the zero-point energy is indeed comparable to the barrier for proton transfer in both **1** and **2**, entirely consistent

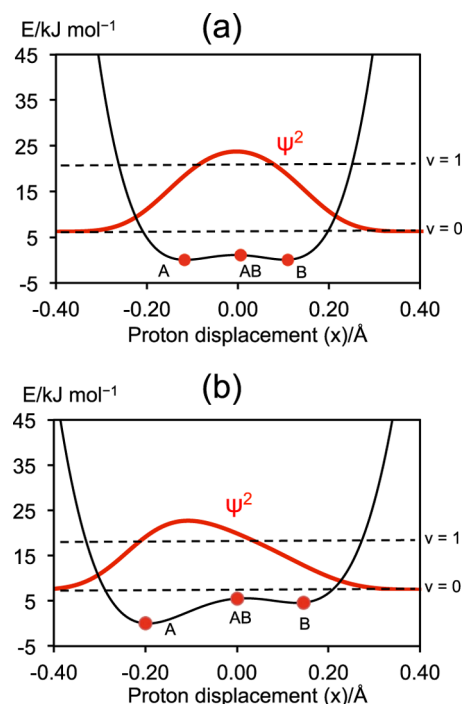


Figure 6. 1D adiabatic potential energy curves for proton transfer and the ground state nuclear probability distributions ($|\Psi|^2$) for simplified linear HB models to mimic (a) **1** and (b) **2**. The proton displacement (x) is defined as the difference between d_{O1H1} and d_{H1O2} . When $x = 0$, the proton is at the midpoint between O1 and O2. The 1D potential energy curves were generated with the following polynomial functions: (a) $y = 7239.092x^4 + 160.464x^3 - 172.415x^2 - 1.795x + 1.088$; (b) $y = 3928.789x^4 + 230.807x^3 - 210.745x^2 + 7.521x + 5.340$. The data points in red mark the positions of models A, AB, and B obtained from CASTEP calculations. The energy values for the ground ($v = 0$) and first excited ($v = 1$) states are: (a) 6.0 and 21.3; (b) 7.3 and 18.0 kJ mol⁻¹.

with the notion of LBHB formation. It is also interesting to note some subtle differences between **1** and **2**. In **1**, the barrier is slightly below the zero-point energy, leading to the situation where the most probable proton position is centered between O1 and O2. In **2**, two different features of the potential energy curve result in a different proton probability distribution. One is the slightly higher energy barrier for proton transfer and the other is the asymmetry between the two local energy minima. Now the proton is significantly shifted toward O1. The smaller energy barrier in **1** is probably because the distance between O1 and O2 in **1** (2.435 Å) is slightly less than that in **2** (2.455 Å). Interestingly, the potential curves shown in Figure 6 are in agreement with what Gilli et al. concluded about the hydrogen bonding in **1**, which they classified as having a weakly asymmetric double minimum with the ZPE greater than the barrier.¹⁰ However, we should also note that the 1D potential curves shown in Figure 6 depend critically on the accuracy of the computed electronic energies in the plane-wave DFT calculations and that, given the assumptions used here, these results are intended only to provide a qualitative description of the nature of the problem.

3.3. Quantum Chemical Calculations of NMR Parameters. In the previous section, we discussed the three structural models for **1** and **2**. Now we report the computed NMR parameters for these models. The results are also summarized in Table 1, where we also showed the results from another

model where the NMR parameters from models A and B are averaged, as if the proton can take two positions (A and B) with equal populations; thus, this model is denoted as model $\langle A + B \rangle$. In principle, the “averaging” should take place along the entire 1D nuclear wavefunction as shown in Figure 6. However, in the absence of detailed information about NMR parameters at each point of the nuclear wavefunction, we may use model $\langle A + B \rangle$ as the simplest way of examining the effect of proton probability distribution. It is important to point out that, to “average” the ^{17}O NMR parameters between A and B, one must consider the orientations of the tensor components in the molecular frame of reference. For this reason, the ^{17}O NMR tensor orientations are depicted in Figure 7.

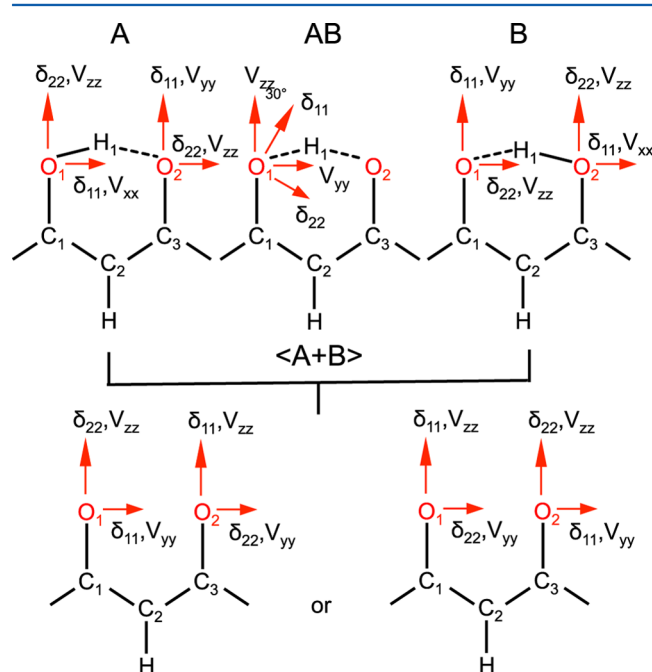


Figure 7. Illustrations of the orientations of the ^{17}O QC and CS tensor components in the molecular frame of reference for models A, AB, B, and $\langle A + B \rangle$ in 1 and 2. In model $\langle A + B \rangle$, as the averaged ^{17}O CS tensors are nearly axially symmetric, two possible relative orientations between the CS and QC are shown. Left: O1, $\alpha = 0$, $\beta = 90^\circ$, $\gamma = 90^\circ$; O2, $\alpha = 0$, $\beta = 90^\circ$, $\gamma = 0^\circ$. Right: O1, $\alpha = 0$, $\beta = 90^\circ$, $\gamma = 0^\circ$; O2, $\alpha = 0$, $\beta = 90^\circ$, $\gamma = 90^\circ$. See the text for discussion.

A careful comparison between the experimental and computational solid-state (^1H , ^{13}C , ^{17}O) NMR results, shown in Table 1 allowed us to draw the following conclusions. First, it is quite clear that neither model A nor B produces NMR parameters that are in satisfactory agreement with the experimental values. This is particularly true for the ^{17}O CS tensor components, as illustrated in Figure 8. Second, overall models AB and $\langle A + B \rangle$ produce very similar NMR parameters that are in reasonable agreement with the experimental ones; see also Figure 8. However, we should point out that, although it may be difficult to differentiate between models AB and $\langle A + B \rangle$, two pieces of evidence point to the direction that favors model $\langle A + B \rangle$ over model AB. We note that, when the proton is near the midpoint between O1 and O2 as is the case in model AB, the ^1H is considerably less shielded (20.2 ppm in 1 and 19.4 ppm in 2) than those seen in model $\langle A + B \rangle$ (19.0 ppm in 1 and 17.1 ppm in 2). The former situation is similar to that observed for potassium hydrogen maleate, $\delta(^1\text{H}) = 20.9$

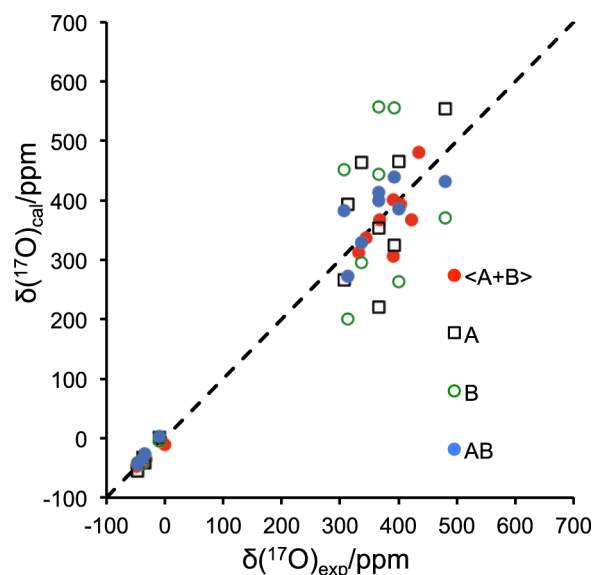


Figure 8. Comparison between the experimental and computed ^{17}O CS tensor components for 1 and 2.

ppm,⁶¹ where the proton has the greatest probability at the midpoint between the two oxygen atoms.^{62–64} Another observation is that the relative orientation between the ^{17}O QC and CS tensors (O1, $\alpha = 0$, $\beta = 90^\circ$, $\gamma = 90^\circ$; O2, $\alpha = 0$, $\beta = 90^\circ$, $\gamma = 0^\circ$) is in better agreement with what model $\langle A + B \rangle$ predicts (O1, $\alpha = 0$, $\beta = 90^\circ$; O2, $\alpha = 0$, $\beta = 90^\circ$, $\gamma = 0^\circ$) than that in model AB (O1 and O2, $\alpha = 0$, $\beta = 90^\circ$, $\gamma = 30^\circ$). Furthermore, as mentioned earlier, model $\langle A + B \rangle$ considers the averaging effect between only two points along the nuclear wavefunctions. It is entirely possible that a correct averaging over the entire nuclear wavefunction shown in Figure 6 would produce improved agreement between calculated and experimental NMR parameters.

The ^2H NMR data deserve further comments. As seen from Table 1, the experimental $C_Q(^2\text{H})$ values for 1 and 2 are substantially different from the computed ones regardless of the model used. Several factors may contribute to the failure for the plane-wave DFT computation to reproduce the experimental ^2H quadrupole parameters. First, the ^2H -labeled compounds may have slightly different equilibrium structural features (such as O...O distances) from the protonated compound. Even a subtle change in structure will have an impact on the hydrogen bonding potential. Second, it may also be necessary to consider the probability distribution of the deuteron in the O...D...O HB to be able to perform averaging over the entire nuclear wavefunction. It is conceivable that the electric-field gradient at the deuteron is an exquisitely sensitive probe of the nuclear wavefunction. Finally, a close inspection of data shown in Table 1 reveals that model A seems to produce the closest results for the ^2H quadrupole parameters for 2. It is entirely possible that because of the asymmetric feature of the hydrogen bonding potential (as shown in Figure 6), the deuteron wavefunction is more localized on one side of the HB. This situation would be better captured in model A.

3.4. Plane-Wave DFT MD Simulations. Although the 1D potential energy curves for proton transfer discussed in the previous section provide useful insights into the nature of the proton probability distribution in 1 and 2, it is nonetheless an oversimplified model. To better understand the 3D PES in the LBHBs in 1 and 2, we performed ab initio MD calculations,

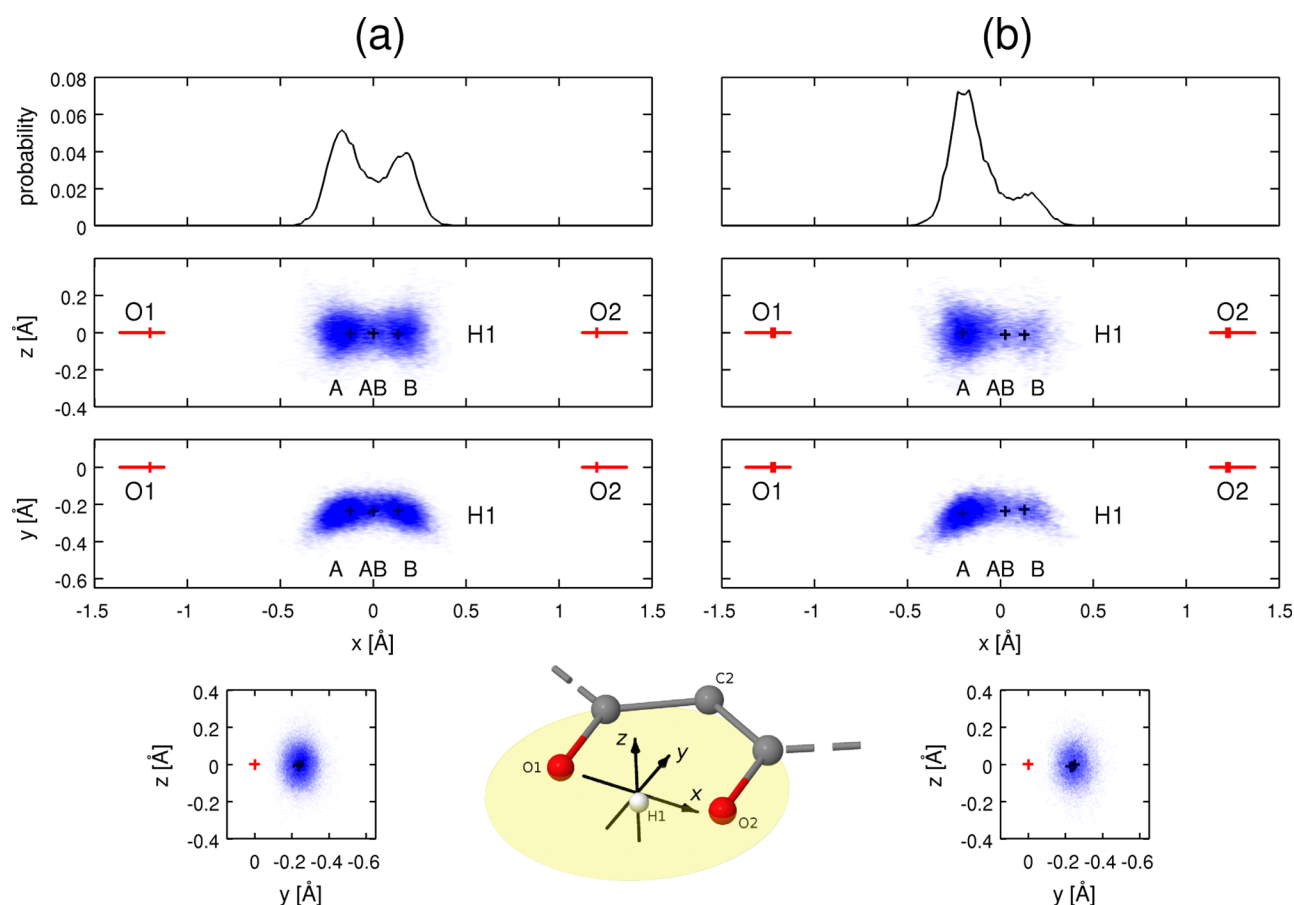


Figure 9. Probability density distributions of H1 in **1** (a) and **2** (b). Each point in the MD trajectory is transformed into the respective coordinate system shown in the inset. The origin of this coordinate system is at the center of mass of the O1 and O2 atoms, and the O1–O2–C2 plane forms the x – y plane. The H1 positions in models A, AB, and B are also marked by “+” (in black) for comparison. The top row shows the integrated projection of the probability density distribution along the y axis and z axis as a function of the x -coordinate.

employing the CASTEP plane-wave DFT code.⁴² It is important to mention that, in these classic *ab initio* MD simulations, the proton is treated as a classic particle without including nuclear quantum effects. Further details of the MD calculations are given in Section 2. In both **1** and **2**, we were particularly interested in the geometry of the intramolecular HB containing O1, H1, and O2 atoms.

Figure 9 shows the three-dimensional probability density distributions of the H1 proton in **1** and **2**. These pictures were generated by transforming the proton position at each point of the MD trajectory into a center-of-mass coordinate system as defined in Figure 9. Remarkably, although these plots represent probability density distributions of a classical *ab initio* MD trajectory, they can to some degree be understood as the visualization of the probability density of the quantum mechanical wavefunction of the H1 proton ($|\Psi|^2$) in the asymmetric LBHB potential. This analogy could be further improved by performing path-integral MD calculations^{18,65,66} but those are significantly more costly in terms of computational time. Nonetheless, the most important finding from the *ab initio* MD simulations is that, in both **1** and **2**, the proton probability distribution is significantly spread out between the O1 and O2 atoms. On the basis of these simulations, although the proton probability distribution is more or less symmetric between O1 and O2 in **1**, it is clearly asymmetric in **2**, having the proton shifting toward O1. The asymmetric proton probability distribution in **2** is intrinsically related to the

asymmetric potential energy curve discussed earlier and the exact shape of the distribution is critically linked to the accuracy of the current plane-wave DFT calculations. One can see from Figure 9 that the proton probability distribution occurs essentially along the direction of the LBHB. For example, the proton probability distribution covers a range of ~ 0.6 Å along the x direction, whereas along both the y and z directions, they are confined to a range of ~ 0.2 Å. This is because the PES for proton motion is relatively flat only along the LBHB direction. The probability function determined from classical MD for both **1** and **2** displays a local minimum for the proton being in the middle of O1 and O2 (defined as model AB in the previous section). This minimum was not seen in the quantum mechanical probability distribution shown in Figure 6. Two important factors may contribute to this discrepancy. First, the 1D proton probability distributions are obtained from oversimplified linear HBs. The full dimensionality of the MD simulations for **1** and **2**, however, takes into consideration cooperative action of all atoms within the molecule. Second, in classical MD, the proton can take all values of the hydrogen bonding potential, whereas in the quantum mechanical description, the proton is restricted to the discrete potential energy states. Hence, in the quantum mechanical picture, the probability function is smeared, leading to a maximum in the middle of O1 and O2 for **1** and a maximum shifted toward O1 for **2**. Performing path-integral MD calculations is expected to lead to results that would resemble those shown in the 1D

models. Kawashima and Tachikawa have compared classical MD and path-integral MD for the case of hydrogen maleate.⁶⁵ Classical MD showed localization of the proton on either oxygen atom, whereas path-integral MD showed localization in the middle of the two oxygens.⁶⁵ As a result, the probability distribution obtained by classical MD reflects more of the hydrogen bonding potential than the quantum mechanical distribution function of the proton.

In addition to the general visualization displayed in Figure 9, we can also obtain detailed information about the LBHBs in **1** and **2** from the MD trajectories. Figure 10 shows the

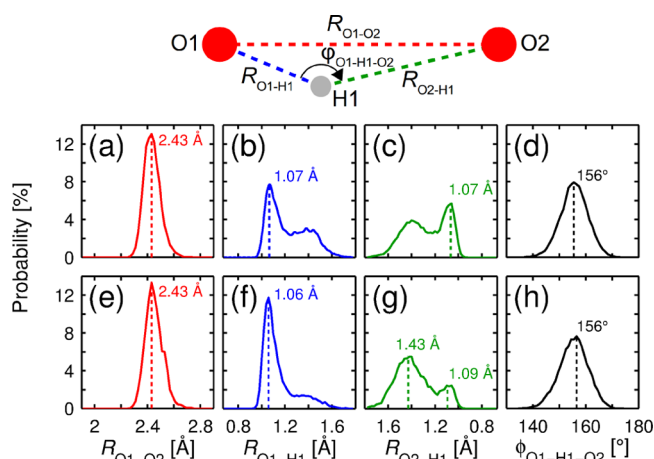


Figure 10. Probability distributions of the O1–O2 distances (a, e), O1–H1 distances (b, f), O2–H1 distances (c, g), and the O1–H1–O2 bond angle (d, h) from ab initio MD calculations in **1** (a–d) and **2** (e–h).

probability distributions of the O1–O2 distance, the O1–H1 distance, the O2–H1 distance, and the O1–H1–O2 bond angle during the MD trajectory for the two compounds. One can see from Figure 10 that the probability distributions for the O1–O2 distance and the O1–H1–O2 bond angle are very similar in **1** and **2**. For example, the values with the highest probability of the O1–O2 distance and the O1–H1–O2 bond angle are 2.43 Å and 156°, respectively, for both compounds. The proton delocalization can also be further quantified by examining the probability distributions of the O1–H1 and O2–H1 distances. In **1**, the distributions of both distances show an overall maximum at 1.07 Å, but the O1–H1 peak is slightly higher than the O2–H1 peak (Figure 10b,c). The situation is very different in **2** where the O1–H1 peak ($d_{\text{O1H1}} = 1.06$ Å) is significantly higher than the O2–H1 peak ($d_{\text{O2H1}} = 1.09$ Å); see Figure 10f,g. This indicates that the asymmetry in the LBHB potential in **2** is significantly greater as illustrated in Figure 6, leading to a higher probability density of the H1 proton close to the O1 oxygen site.

3.5. General Discussion on Proton Probability Distribution in LBHBs. It is well established that the shape of a HB potential depends critically on the distance between the HB donor and acceptor atoms.^{12–14} For neutral OHO HBs, three general types of HB potentials are (1) single-well potential (or double-well with the barrier height significantly below the ZPE), (2) LBHB, and (3) double-well potential with the barrier height being higher than the ZPE. As we discussed in the previous section, the proton probability distributions shown in Figure 9 should be treated as a general feature of all LBHBs. If we use this feature as a strict criterion for LBHB

formation, it is clear that not all 1,3-diketones would form an LBHB. For example, in the gas phase, the *cis*-keto–enol tautomer of acac exhibits an intramolecular HB with an O...O distance of 2.592 Å, as determined from a recent electron diffraction study.¹⁶ A high-level quantum chemical calculation suggests that acac has a double-well HB potential with a barrier height of 15.27 kJ mol^{−1}.¹⁷ In this case, because the barrier height is greater than the ZPE by 8.26 kJ mol^{−1}, the proton should be considered to be dynamically averaged through quantum tunneling between the two *cis*-keto–enol tautomers (i.e., O–H...O ⇌ O...H–O). In each tautomer, the proton is directly bonded to one oxygen atom. Indeed, an early gas-phase ¹H NMR study showed that the proton involved in the intramolecular HB in acac has a chemical shift of 15.2 ppm.⁶ Thus, we should distinguish between the HB in acac and those seen in **1** and **2** in the solid state. We also know that when the proton is in the middle of a single-well potential, its ¹H chemical shift is usually about 19–20 ppm. Therefore, it seems that **1** and **2** are indeed good examples of LBHB formation. In some aspects, the LBHB in **2** exhibits similarities with that in benzoylacetone for which $\delta(^1\text{H}) = 16.2$ ppm and $r_{\text{OO}} = 2.502$ Å.^{20,67} The Carr–Parrinello MD simulations of benzoylacetone in the solid state showed a 1D free-energy profile for proton transfer similar to that seen for **2** (Figure 6b).⁶⁸ However, the authors also showed that the inclusion of the nuclear quantum effect in their path-integral MD simulations for benzoylacetone significantly reduces the barrier height, resulting in a slightly asymmetric single-minimum potential. Here, it is worth pointing out that one should not confuse this single-minimum potential in benzoylacetone with that seen in hydrogen maleate, another well-known system having a HB with a single-minimum potential. Because the hydrogen bonding interactions in these two compounds are clearly different, as evidenced by the very different ¹H chemical shifts in the two cases (20.9 ppm in hydrogen maleate vs 16.2 ppm in benzoylacetone), an oversimplified description whether a H-bond has either a single- or double-minimum potential is insufficient to capture the details of the H-bond. For example, the detailed 2D free-energy landscape obtained for benzoylacetone from the path-integral MD simulation is distinctly different from that for hydrogen maleate from similar MD simulations.⁶⁵ Thus, one must examine the detailed 3D proton probability distribution in each case.

4. CONCLUSIONS

In this work, we reported solid-state ¹H, ²H, ¹³C, and ¹⁷O NMR results for two 1,3-diketones where intramolecular LBHBs are present. Combining experimental solid-state NMR results with ab initio MD simulations has allowed us to obtain a detailed picture about the proton probability distribution across the LBHBs in these compounds. The origin of such a proton probability distribution is the nuclear quantum effect. We showed that, although the ab initio MD simulation methodology employed in this study treats the proton in question as a classic particle, the flat PES across the LBHBs in **1** and **2** allows sufficient sampling in the configuration space, thus mapping out a proton probability density distribution that qualitatively resembles the nuclear wavefunction for zero-point motion. Further improvement of such distributions can be achieved by performing ab initio path-integral MD simulations. Our results suggest that proton probability distribution is an intrinsic feature of an LBHB and should form the basis for understanding different (sometimes contradicting) results obtained

by complementary experimental techniques such as solid-state NMR, X-ray or neutron diffraction, IR, elastic neutron scattering, and so forth. It is also important to emphasize that, as the shape of the HB potential depends critically on the HB distance, care must be exercised when comparing experimental and computational results obtained from different phases (gas, liquid, and solid) and under different experimental conditions (e.g., temperature, pressure, etc.).

■ ASSOCIATED CONTENT

Supporting Information

The Supporting Information is available free of charge on the ACS Publications website at DOI: 10.1021/acs.jpcb.6b08091.

A list of complete experimental and calculated ^{13}C isotropic chemical shifts for **1** and **2**; a correlation plot comparing the experimental and calculated ^{13}C chemical shifts in **1** and **2**; variable-temperature ^{17}O MAS spectra for **1** and **2** recorded at 21.1 T (PDF)

■ AUTHOR INFORMATION

Corresponding Authors

*E-mail: andreas.brinkmann@nrc-cnrc.gc.ca (A.B.).

*E-mail: roderick.wasylishen@ualberta.ca (R.E.W.).

*E-mail: gang.wu@chem.queensu.ca (G.W.).

Notes

The authors declare no competing financial interest.

■ ACKNOWLEDGMENTS

This work was supported by the Natural Sciences and Engineering Research Council (NSERC) of Canada. Access to the 900 MHz NMR spectrometer was provided by the National Ultrahigh Field NMR Facility for Solids (Ottawa, Canada), a national research facility supported by a consortium of Canadian universities, National Research Council Canada and Bruker BioSpin and managed by the University of Ottawa (<http://nmr900.ca>). We thank Prof. Brian A. Pettitt (University of Winnipeg) for helpful discussions concerning hydrogen bonding as well as Prof. Glenn Penner (University of Guelph) for obtaining deuterium NMR spectra of ^2H -labeled curcumin. We also thank Prof. Tucker Carrington for helpful discussions about nuclear quantum effects.

■ REFERENCES

- (1) Emsley, J. The composition, structure and hydrogen bonding of the β -diketones. In *Structure and Bonding*; Emsley, J., Ernst, R. D., Hathaway, B. J., Warren, K. D., Eds.; Springer: Berlin Heidelberg, 1984; Vol. 57, pp 147–191.
- (2) Hibbert, F.; Emsley, J. Hydrogen bonding and chemical reactivity. In *Advances in Physical Organic Chemistry*; Bethell, D., Ed.; Academic Press Inc.: San Diego, CA, 1991; Vol. 26, pp 255–379.
- (3) Grushow, A.; Zielinski, T. J. Hydrogen bonding using NMR: A new look at the 2,4-pentanedione keto-enol tautomer experiment. *J. Chem. Educ.* **2002**, *79*, 707–714.
- (4) Nichols, M. A.; Waner, M. J. Kinetic and mechanistic studies of the deuterium exchange in classical keto-enol tautomeric equilibrium reactions. *J. Chem. Educ.* **2010**, *87*, 952–955.
- (5) Sandusky, P. O. Expansion of the classic acetylacetone physical chemistry laboratory NMR experiment: Correlation of the enol-keto equilibrium position with the solvent dipole moment. *J. Chem. Educ.* **2014**, *91*, 739–742.
- (6) Folkendt, M. M.; Weiss-Lopez, B. E.; Chauvel, J. P., Jr.; True, N. S. Gas-phase proton NMR studies of keto-enol tautomerism of acetylacetone, methyl acetoacetate, and ethyl acetoacetate. *J. Phys. Chem.* **1985**, *89*, 3347–3352.
- (7) Rogers, M. T.; Burdett, J. L. Keto-enol tautomerism in β -dicarbonyls studied by nuclear magnetic resonance spectroscopy: II. Solvent effects on proton chemical shifts and on equilibrium constants. *Can. J. Chem.* **1965**, *43*, 1516–1526.
- (8) Camerman, A.; Mastropaolo, D.; Camerman, N. Molecular structure of acetylacetone. A crystallographic determination. *J. Am. Chem. Soc.* **1983**, *105*, 1584–1586.
- (9) Gilli, G.; Bellucci, F.; Ferretti, V.; Bertolasi, V. Evidence for resonance-assisted hydrogen bonding from crystal-structure correlations on the enol form of the β -diketone fragment. *J. Am. Chem. Soc.* **1989**, *111*, 1023–1028.
- (10) Gilli, P.; Bertolasi, V.; Pretto, L.; Ferretti, V.; Gilli, G. Covalent versus electrostatic nature of the strong hydrogen bond: Discrimination among single, double, and asymmetric single-well hydrogen bonds by variable-temperature X-ray crystallographic methods in β -diketone enol RAHB systems. *J. Am. Chem. Soc.* **2004**, *126*, 3845–3855.
- (11) Boese, R.; Antipin, M. Y.; Bläser, D.; Lyssenko, K. A. Molecular crystal structure of acetylacetone at 210 and 110 K: Is the crystal disorder static or dynamic? *J. Phys. Chem. B* **1998**, *102*, 8654–8660.
- (12) Somorjai, R. L.; Hornig, D. F. Double-minimum potentials in hydrogen-bonded solids. *J. Chem. Phys.* **1962**, *36*, 1980–1987.
- (13) Perrin, C. L.; Nielson, J. B. “Strong” hydrogen bonds in chemistry and biology. *Annu. Rev. Phys. Chem.* **1997**, *48*, 511–544.
- (14) McKenzie, R. H.; Bekker, C.; Athokpam, B.; Ramesh, S. G. Effect of quantum nuclear motion on hydrogen bonding. *J. Chem. Phys.* **2014**, *140*, No. 174508.
- (15) Caminati, W.; Grabow, J.-U. The C_{2v} structure of enolic acetylacetone. *J. Am. Chem. Soc.* **2006**, *128*, 854–857.
- (16) Srinivasan, R.; Feenstra, J. S.; Park, S. T.; Xu, S.; Zewail, A. H. Direct determination of hydrogen-bonded structures in resonant and tautomeric reactions using ultrafast electron diffraction. *J. Am. Chem. Soc.* **2004**, *126*, 2266–2267.
- (17) Broadbent, S. A.; Burns, L. A.; Chatterjee, C.; Vaccaro, P. H. Investigation of electronic structure and proton transfer in ground state acetylacetone. *Chem. Phys. Lett.* **2007**, *434*, 31–37.
- (18) Li, X.-Z.; Walker, B.; Michaelides, A. Quantum nature of the hydrogen bond. *Proc. Natl. Acad. Sci. U.S.A.* **2011**, *108*, 6369–6373.
- (19) Thomas, L. H.; Florence, A. J.; Wilson, C. C. Hydrogen atom behaviour imaged in a short intramolecular hydrogen bond using the combined approach of X-ray and neutron diffraction. *New J. Chem.* **2009**, *33*, 2486–2490.
- (20) Emmmler, Th.; Gieschler, S.; Limbach, H. H.; Buntkowsky, G. A simple method for the characterization of OHO-hydrogen bonds by ^1H -solid state NMR spectroscopy. *J. Mol. Struct.* **2004**, *700*, 29–38.
- (21) Etter, M. C.; Reutzel, S. M.; Vojta, G. M. Analysis of isotropic chemical shift data from high-resolution solid-state NMR studies of hydrogen-bonded organic compounds. *J. Mol. Struct.* **1990**, *237*, 165–185.
- (22) Vila, A. J.; Lagier, C. M.; Olivieri, A. C. ^{13}C NMR and AM1 study of the intramolecular proton transfer in solid 1,3-diphenylpropane-1,3-dione. *J. Chem. Soc. Perkin Trans. 2* **1990**, 1615–1618.
- (23) Jones, R. D. G. The crystal structure of the enol tautomer of 1,3-diphenyl-1,3-propanedione (dibenzoylmethane) by neutron diffraction. *Acta Crystallogr., Sect. B: Struct. Sci., Cryst. Eng. Mater.* **1976**, *32*, 1807–1811.
- (24) Aliev, A. E.; Harris, K. D. M. Probing Hydrogen Bonding in Solids Using Solid State NMR Spectroscopy. In *Supramolecular Assembly via Hydrogen Bonds I*; Mingos, D. M. P., Ed.; Springer: Berlin, 2004; Vol. 108, pp 1–53.
- (25) Brunner, E.; Sternberg, U. Solid-state NMR investigations on the nature of hydrogen bonds. *Prog. Nucl. Magn. Reson. Spectrosc.* **1998**, *32*, 21–57.
- (26) Lorente, P.; Shenderovich, I. G.; Golubev, N. S.; Denisov, G. S.; Buntkowsky, G.; Limbach, H.-H. $^1\text{H}/^{15}\text{N}$ NMR chemical shielding, dipolar $^{15}\text{N}, ^2\text{H}$ coupling and hydrogen bond geometry correlations in a novel series of hydrogen-bonded acid–base complexes of collidine with carboxylic acids. *Magn. Reson. Chem.* **2001**, *39*, S18–S29.

- (27) Brown, S. P. Hydrogen bonding in crystalline organic solids. In *Encyclopedia of Magnetic Resonance*; Harris, R. K.; Wasylishen, R. E., Eds.; John Wiley: Chichester, Posted on-line December 15, 2008. DOI: 10.1002/9780470034590.emrstm1006.
- (28) Wu, G. Solid-state ^{17}O NMR studies of organic and biological molecules. *Prog. Nucl. Magn. Reson. Spectrosc.* **2008**, *52*, 118–169.
- (29) Etter, M. C.; Jahn, D. A.; Urbańczyk-Lipkowska, Z. A new polymorph of dibenzoylmethane. *Acta Crystallogr., Sect. C: Cryst. Struct. Commun.* **1987**, *43*, 260–263.
- (30) Kaitner, B.; Mestrovic, E. Structure of a new crystal modification of 1,3-diphenyl-1,3-propanedione. *Acta Crystallogr., Sect. C: Cryst. Struct. Commun.* **1993**, *49*, 1523–1525.
- (31) Goel, A.; Kunnumakara, A. B.; Aggarwal, B. B. Curcumin as “Curcumin”: From kitchen to clinic. *Biochem. Pharmacol.* **2008**, *75*, 787–809.
- (32) Gupta, S. C.; Kismali, G.; Aggarwal, B. B. Curcumin, a component of turmeric: From farm to pharmacy. *BioFactors* **2013**, *39*, 2–13.
- (33) Bairwa, K.; Grover, J.; Kania, M.; Jachak, S. M. Recent developments in chemistry and biology of curcumin analogues. *RSC Adv.* **2014**, *4*, 13946–13978.
- (34) Tonnesen, H. H.; Karlsen, J.; Mostad, A. Structural studies of curcuminoids. I. The crystal structure of curcumin. *Acta Chem. Scand., Ser. B* **1982**, *36*, 475–479.
- (35) Parimita, S. P.; Ramshankar, Y. V.; Suresh, S.; Row, T. N. G. Redetermination of curcumin: (1E, 4Z, 6E)-5-hydroxy-1,7-bis(4-hydroxy-3-methoxyphenyl)hepta-1,4,6-trien-3-one. *Acta Crystallogr., Sect. E: Struct. Rep. Online* **2007**, *63*, o860–o862.
- (36) Sanphui, P.; Goud, N. R.; Khandavilli, U. B. R.; Nangia, A. Fast dissolving curcumin cocrystals. *Cryst. Growth Des.* **2011**, *11*, 4135–4145.
- (37) Zhao, X.-Z.; Jiang, T.; Wang, L.; Yang, H.; Zhang, S.; Zhou, P. Interaction of curcumin with Zn(II) and Cu(II) ions based on experiment and theoretical calculation. *J. Mol. Struct.* **2010**, *984*, 316–325.
- (38) Cornago, P.; Cabildo, P.; Sanz, D.; Claramunt, R. M.; Torralba, M. C.; Torres, M. R.; Elguero, J. Structures of hemi-curcuminoids in the solid state and in solution. *Eur. J. Org. Chem.* **2013**, 6043–6054.
- (39) Sanphui, P.; Goud, N. R.; Khandavilli, U. B. R.; Bhanoth, S.; Nangia, A. New polymorphs of curcumin. *Chem. Commun.* **2011**, *47*, 5013–5015.
- (40) Liu, J.; Svård, M.; Hippen, P.; Rasmuson, Å. C. Solubility and crystal nucleation in organic solvents of two polymorphs of curcumin. *J. Pharm. Sci.* **2015**, *104*, 2183–2189.
- (41) Massiot, D.; Fayon, F.; Capron, M.; King, I.; Le Calvé, S.; Alonso, B.; Durand, J.-O.; Bujoli, B.; Gan, Z.; Hoatson, G. Modelling one- and two-dimensional solid-state NMR spectra. *Magn. Reson. Chem.* **2002**, *40*, 70–76.
- (42) Clark, S. J.; Segall, M. D.; Pickard, C. J.; Hasnip, P. J.; Probert, M. I. J.; Refson, K.; Payne, M. C. First principles methods using CASTEP. *Z. Kristallogr.* **2005**, *220*, 567–570.
- (43) Perdew, J. P.; Burke, K.; Ernzerhof, M. Generalized gradient approximation made simple. *Phys. Rev. Lett.* **1996**, *77*, 3865–3868.
- (44) Pickard, C. J.; Mauri, F. All-electron magnetic response with pseudopotentials: NMR chemical shifts. *Phys. Rev. B* **2001**, *63*, No. 245101.
- (45) Yates, J. R.; Pickard, C. J.; Mauri, F. Calculation of NMR chemical shifts for extended systems using ultrasoft pseudopotentials. *Phys. Rev. B* **2007**, *76*, No. 024401.
- (46) Etter, M. C.; Vojta, G. M.; Bronniman, C. E. Combined use of ^1H CRAMPS NMR and X-ray crystallography to detect a strong intramolecular aromatic shielding effect in 2-acetyl-1,3-diphenyl-1,3-propanedione. *J. Magn. Reson.* **1991**, *93*, 609–613.
- (47) Jameson, C. J.; Gutowsky, H. S. Calculation of chemical shifts. I. General formulation and the Z dependence. *J. Chem. Phys.* **1964**, *40*, 1714–1724.
- (48) Barnes, R. G.; Smith, W. V. Electric field gradients of atomic p electrons. *Phys. Rev.* **1954**, *93*, 95–98.
- (49) Kwan, I. C. M.; Mo, X.; Wu, G. Probing hydrogen bonding and ion-carbonyl interactions by solid-state ^{17}O NMR spectroscopy: G-ribbon and G-quartet. *J. Am. Chem. Soc.* **2007**, *129*, 2398–2407.
- (50) Zhu, J.; Geris, A. J.; Wu, G. Solid-state ^{17}O NMR as a sensitive probe of keto and gem-diol forms of α -keto acid derivatives. *Phys. Chem. Chem. Phys.* **2009**, *11*, 6972–6980.
- (51) Zhu, J.; Lau, J. Y. C.; Wu, G. A solid-state ^{17}O NMR study of L-tyrosine in different ionization states: Implications for probing tyrosine side chains in proteins. *J. Phys. Chem. B* **2010**, *114*, 11681–11688.
- (52) Yamada, K.; Dong, S.; Wu, G. Solid-state ^{17}O NMR investigation of the carbonyl oxygen electric-field-gradient tensor and chemical shielding tensor in amides. *J. Am. Chem. Soc.* **2000**, *122*, 11602–11609.
- (53) Brown, T. L.; Butler, L. G.; Curtin, D. Y.; Hiyama, Y.; Paul, I. C.; Wilson, R. B. Deuterium nuclear quadrupole resonance spectra of nonlinear hydrogen bonds. *J. Am. Chem. Soc.* **1982**, *104*, 1172–1177.
- (54) Zhao, X.; Rossi, P.; Barsegov, V.; Zhou, J.; Woodford, J. N.; Harbison, G. S. Temperature dependent deuterium quadrupole coupling constants of short hydrogen bonds. *J. Mol. Struct.* **2006**, *790*, 152–159.
- (55) Berglund, B.; Vaughan, R. W. Correlations between proton chemical shift tensors, deuterium quadrupole couplings, and bond distances for hydrogen bonds in solids. *J. Chem. Phys.* **1980**, *73*, 2037–2043.
- (56) Wong, A.; Smith, M. E.; Terskikh, V.; Wu, G. Obtaining accurate chemical shifts for all magnetic nuclei (^1H , ^{13}C , ^{17}O , and ^{27}Al) in tris(2,4-pentanedionato- O, O')aluminum(III)—A solid-state NMR case study. *Can. J. Chem.* **2011**, *89*, 1087–1094.
- (57) Deringer, V. L.; Hoepfner, V.; Dronskowski, R. Accurate hydrogen positions in organic crystals: Assessing a quantum-chemical aide. *Cryst. Growth Des.* **2012**, *12*, 1014–1021.
- (58) Kong, X.; Shan, M.; Terskikh, V.; Hung, I.; Gan, Z.; Wu, G. Solid-state ^{17}O NMR of pharmaceutical compounds: Salicylic acid and aspirin. *J. Phys. Chem. B* **2013**, *117*, 9643–9654.
- (59) Mori, Y.; Masuda, Y. Effect of solvent on proton location and dynamic behavior in short intramolecular hydrogen bonds studied by molecular dynamics simulations and NMR experiments. *Chem. Phys.* **2015**, *458*, 18–29.
- (60) Levine, I. N. Numerical solution of the one-dimensional time-independent Schrödinger equation. In *Quantum Chemistry*, 7th ed.; Pearson, 2014; Chapter 4.4.
- (61) Achlama, A. M.; Kohlschütter, U.; Haeberlen, U. Proton shielding tensors in potassium hydrogen maleate. *Chem. Phys.* **1975**, *7*, 287–293.
- (62) Darlow, S. F.; Cochran, W. The crystal structure of potassium hydrogen maleate. *Acta Crystallogr.* **1961**, *14*, 1250–1257.
- (63) Darlow, S. F. The configuration of the strained hydrogen maleate ion. *Acta Crystallogr.* **1961**, *14*, 1257–1259.
- (64) Peterson, S. W.; Levy, H. A. Structure of potassium hydrogen maleate by neutron diffraction. *J. Chem. Phys.* **1958**, *29*, 948–949.
- (65) Kawashima, Y.; Tachikawa, M. Nuclear quantum effect on intramolecular hydrogen bond of hydrogen maleate anion: An ab initio path integral molecular dynamics study. *Chem. Phys. Lett.* **2013**, *571*, 23–27.
- (66) Dračinský, M.; Bouř, P.; Hodgkinson, P. Temperature dependence of NMR parameters calculated from path integral molecular dynamics simulations. *J. Chem. Theory Comput.* **2016**, *12*, 968–973.
- (67) Herstein, F. H.; Iversen, B. B.; Kapon, M.; Larsen, F. K.; Madsen, G. K. H.; Reisner, G. M. X-ray and neutron diffraction study of benzoylacetone in the temperature range 8–300 K: comparison with other *cis-enol* molecules. *Acta Crystallogr., Sect. B: Struct. Sci., Cryst. Eng. Mater.* **1999**, *55*, 767–787.
- (68) Durlak, P.; Latajka, Z. Car–Parrinello and path integral molecular dynamics study of the intramolecular hydrogen bonds in the crystals of benzoylacetone and dideuterobenzoylacetone. *Phys. Chem. Chem. Phys.* **2014**, *16*, 23026–23037.